Ab-initio calculation of total x-ray scattering from molecules

Ab-initio calculation of total x-ray scattering from molecules

Andrés Moreno Carrascosa,[†] Haiwang Yong,[‡] Deborah L. Crittenden,[¶] Peter M. Weber,[‡] and Adam Kirrander[*,†]

[†]*EaStChem, School of Chemistry, University of Edinburgh, David Brewster Road, EH9 3FJ Edinburgh, United Kingdom*
[‡]*Department of Chemistry, Brown University, Providence, Rhode Island 02912, USA*
[¶]*Department of Chemistry, University of Canterbury, Private Bag 4800, Christchurch 8041, New Zealand*

E-mail: Adam.Kirrander@ed.ac.uk

Abstract

We present a method to calculate total x-ray scattering cross sections directly from *ab-initio* electronic wavefunctions in atoms and molecules. The approach can be used in conjunction with multi-configurational wavefunctions and exploits analytical integrals of Gaussian-type functions over the scattering operator, which leads to accurate and efficient calculations. The results are validated by comparison to experimental results and previous theory for the molecules H_2 and CO_2. Importantly, we find that the inelastic component of the total scattering varies strongly with molecular geometry. The method is appropriate for use in conjunction with quantum molecular dynamics simulations for the analysis of new ultrafast x-ray scattering experiments, and to interpret accurate gas-phase scattering experiments.

1 Introduction

New X-ray Free-Electron Lasers (XFELs) generate large numbers of photons and short duration pulses[1–7] that enable time-resolved x-ray scattering,[8–14] and thus ultrafast imaging of photochemical dynamics.[15] An attractive feature of such experiments is that they provide direct access to the evolution of molecular geometry via the elastic component of the scattering.[16] However, in virtually all instances, the experiments actually measure the *total* scattering, and it is therefore imperative to develop methods to calculate this quantity efficiently and accurately.

Calculations of total scattering have played an important role historically,[17–22] due to influential experimental measurements of static x-ray and electron scattering from gas-phase samples,[23–26] and because the total scattering is strongly influenced by electron correlation which provided fundamental theoretical interest. The prospect of new ultrafast x-ray scattering experiments and the equally rapid developments in ultrafast electron diffraction[27–29] bring new interest to this topic. In the context of ultrafast processes, distorted geometries and quantum dynamics are important, making both the efficiency and the accuracy of the calculations critical for the interpretation of new state-of-the-art experiments.

In the following, we outline a method for the calculation of total scattering from *ab-initio* electronic wavefunctions, based on our previously developed code for the prediction of elastic[30–32] and inelastic[33] scattering[a]. The elastic scattering calculations in particular can be seen as a continuation of pioneering work by Techert and col-

[a]Interestingly, the coherence and short pulse duration of XFELs can lead to interference effects involving inelastic scattering matrix elements when scattering from coherent wavepackets is considered.[34–38]

leagues.[39–41] An important objective is to match the level of accuracy required for quantum molecular dynamics simulations of photochemical reactions,[37] which generally implies a high-level multiconfigurational description of the electronic structure (e.g. CASSCF, CASPT2, or MRCI). Such multi-reference methods will also yield better predictions of the total x-ray scattering due to an improved description of the electron correlation. In the following, we will outline the theory, present our computational approach, demonstrate that we can calculate total scattering accurately, and show that contrary to common assumptions the inelastic component of the scattering varies strongly with molecular geometry.

2 Theory

2.1 X-ray Scattering

The double differential cross section for x-ray scattering in the first Born approximation is,[42]

$$\frac{d^2\sigma}{d\Omega dE_1} = r_0^2 \left(\frac{E_1}{E_0}\right) |\mathbf{e}_0 \cdot \mathbf{e}_1^*|\, S(\mathbf{q}, E'), \qquad (1)$$

where $r_0 = e^2/m_e c^2$ is known as the classical electron radius (e signifies the charge and m_e the mass of an electron, and c the speed of light), E_1 and E_0 are the energies of the scattered and incident x-ray photons, $|\mathbf{e_0} \cdot \mathbf{e_1^*}|$ is the polarization factor, and $S(\mathbf{q}, E')$ is the dynamic structure factor with $E' = E_0 - E_1$. The scattering (or momentum transfer) vector, $\mathbf{q} = \mathbf{k}_0 - \mathbf{k}_1$, is defined as the difference between the incident and the scattered wave vectors, with $k_0 = k_1 + (E'/\hbar c)$.

The dynamic structure factor describes the material response and is given by,

$$S(\mathbf{q}, E') = \sum_\beta \left|\langle \Psi_\beta |\, \hat{L}\, | \Psi_\alpha \rangle\right|^2 \, \delta(E_\beta - E_\alpha - E'), \quad (2)$$

where $|\Psi_\beta\rangle$ and $|\Psi_\alpha\rangle$ are the final and initial states, and $\hat{L}$ is the scattering operator,

$$\hat{L} = \sum_{j=1}^{N} e^{\imath \mathbf{q} \mathbf{r_j}}, \qquad (3)$$

with the sum running over all N electrons in the molecule and $\mathbf{r}_j$ the coordinates of the electrons. The matrix elements $\langle \Psi_\beta |\, \hat{L}\, | \Psi_\alpha \rangle$ in Eq. (2) originate from the $\vec{\mathbf{A}} \cdot \vec{\mathbf{A}}$ terms in the interaction Hamiltonian taken in first order of perturbation theory, with $\vec{\mathbf{A}}$ the vector potential of the electromagnetic field.[42]

Waller and Hartree proposed an approximation, valid in the high photon energy limit (i.e. hard x-rays), whereby the ratio E_1/E_0 in Eq. (1) is taken to be unity.[43] Under this assumption, integration of Eq. (1) over all scattered energies E_1 is straightforward and yields the differential cross section for *total scattering* as,

$$\frac{d\sigma}{d\Omega} = r_0^2 \, |\mathbf{e}_0 \cdot \mathbf{e}_1^*|\, S(\mathbf{q}), \qquad (4)$$

where the dynamic structure factor for total scattering, $S(\mathbf{q})$, is now independent of the energy E' and is given by,

$$S(\mathbf{q}) = \sum_\beta \left|\langle \Psi_\beta |\, \hat{L}\, | \Psi_\alpha \rangle\right|^2 = \langle \Psi_\alpha |\, \hat{L}^\dagger \hat{L}\, | \Psi_\alpha \rangle, \quad (5)$$

where the second equality exploits the closure relation for electronic states $\hat{\mathbf{1}} = \sum_\beta |\Psi_\beta\rangle\langle\Psi_\beta|$. This is a powerful result, since it allows the total scattering from a particular electronic state to be calculated without reference to any other electronic states.

The expression for $S(\mathbf{q})$ in Eq. (5) can be rewritten as a Fourier transform of the reduced two-electron density matrix $\Gamma(\mathbf{r}_1, \mathbf{r}_2)$, which yields,

$$S(\mathbf{q}) = \iint \Gamma(\mathbf{r}_1, \mathbf{r}_2)\, e^{\imath \mathbf{q}(\mathbf{r}_1 - \mathbf{r}_2)}\, d\mathbf{r}_1 d\mathbf{r}_2 \;+\; N, \quad (6)$$

where N is the number of electrons in the molecule as before. The appearance of the two-electron density in Eq. (6) hints at the importance of electron correlation for total scattering.[17,26] In contrast, the elastic component is proportional to the $\langle \Psi_\alpha |\, \hat{L}\, | \Psi_\alpha \rangle$ (i.e. $\beta = \alpha$) term in the sum in Eq. (5), which corresponds to the Fourier transform of the electron density given by the single-electron operator $\hat{\rho}(\mathbf{r}) = \sum_{j=1}^{N} \delta(\mathbf{r} - \mathbf{r}_j)$,

$$F(\mathbf{q}) = \langle \Psi_\alpha |\, \hat{L}\, | \Psi_\alpha \rangle = \int \rho^{(N)}(\mathbf{r})\, e^{\imath \mathbf{q} \mathbf{r}}\, d\mathbf{r}, \qquad (7)$$

where $F(\mathbf{q})$ is known as the form factor and $\rho^{(N)}(\mathbf{r})$

is the electron density. It is common to define the total *inelastic* scattering, $S_{\text{inel}}(\mathbf{q})$, as the difference between the total scattering and the elastic scattering, i.e.

$$S_{\text{inel}}(\mathbf{q}) = S(\mathbf{q}) - |F(\mathbf{q})|^2 . \tag{8}$$

The limits for the elastic and inelastic components with respect to the amplitude of the momentum transfer vector, $q = |\mathbf{q}|$, are $F(0) = S_{\text{inel}}(\infty) = N$ and $F(\infty) = S_{\text{inel}}(0) = 0$.

The orientation of the molecules is isotropic for thermal liquids and gases, in which case the directional dependence of $\mathbf{q}$ is lost and the signal must be rotationally averaged. The rotational averaging $\langle \cdots \rangle_\Omega$ can be done separately for the elastic and total scattering, $|F(q)|^2 = \langle |F(\mathbf{q})|^2 \rangle_\Omega$ and $S(q) = \langle S(\mathbf{q}) \rangle_\Omega$. In principle, more accurate results are obtained using a coherent integration over the rotational wavefunctions of the molecules[21,22,32] but this is only mandated in very specific situations involving e.g. a polarized or state-selected gas.[32] Recently, Parrish and Martínez have also proposed an efficient grid-based method for rotational averaging of *ab-initio* elastic scattering.[44]

All the results discussed above are directly transferable to the scattering of high energy electrons[23,25,26,33,45] if the Thomson differential cross section is replaced by the corresponding Rutherford cross section and additional elastic scattering terms due to electron scattering from the nuclei are included, leading to nuclear-nuclear and nuclear-electronic interference terms.[26] The inelastic contributions are identical for scattering of x-rays and high energy electrons.[25,33]

2.2 Total x-ray scattering matrix elements

To fully account for static electron correlation in atoms and molecules, a multiconfigurational expansion of the wavefunction is required. Such a wavefunction is constructed by distributing the valence electrons over different configurations. Each configuration, represented by Slater determinants or configurations state functions, contributes to the total wavefunction $|\Psi_\alpha\rangle$,

$$|\Psi_\alpha\rangle = \sum_{i=1}^{N_{\text{conf}}} c_{\alpha,i} |\Phi_{\text{SD}}^{\alpha,i}\rangle, \tag{9}$$

where the $c_{\alpha,i}$ are the configuration interaction coefficients for the electronic state α, N_{conf} is the number of configurations included in the expansion, and $|\Phi_{\text{SD}}^{\alpha,i}\rangle$ are the Slater determinants. Slater determinants result from,

$$|\Phi_{\text{SD}}^{\alpha,i}\rangle = (N!)^{-1/2} \sum_{n=1}^{N!} (-1)^{p_n} \mathcal{P}_n \Phi_H^i, \tag{10}$$

with $\mathcal{P}_n$ the pair-wise permutation operator acting on the Hartree product $\Phi_H^i = \chi_1^i(\mathbf{r}_1, \omega_1) \ldots \chi_N^i(\mathbf{r}_N, \omega_N)$ where $\mathbf{r}_j$ are the spatial electron coordinates and ω_j the spin coordinates. The spin orbitals $\chi_j^i(\mathbf{r}_j, \omega_j)$ are the products of the spin functions, $|\uparrow\rangle$ or $|\downarrow\rangle$, and the orthonormal spatial molecular orbitals, $\phi_j^i(\mathbf{r}_j)$, used to construct each Slater determinant[b]. The number of Slater determinants used to construct the wave function will determine the accuracy of the wave function. Further corrections are often required in order to fully consider electron correlation, for instance using a coupled cluster (CC) approach.

According to Eqs. (5-6), the total scattering is given by applying the two-particle scattering operator to the wavefunction, which yields a Fourier transform of the two-electron reduced density matrix. The multiconfigurational two-electron reduced density matrix for a specific electronic state reads,[46]

$$\Gamma(\mathbf{r}_1, \mathbf{r}_2) = \sum_{i=1}^{N_{\text{conf}}} c_{\alpha,i}^2 \sum_{klmn}^{N_{\text{orb}}} \gamma_{klmn} \phi_k^i(\mathbf{r}_1) \phi_l^i(\mathbf{r}_1) \phi_m^i(\mathbf{r}_2) \phi_n^i(\mathbf{r}_2), \tag{11}$$

where $c_{\alpha,i}$ and N_{conf} are defined in Eq. (9), γ_{klmn} are the two-electron reduced density matrix elements, and N_{orb} is the number of spin-orbitals $\phi_j^i(\mathbf{r})$ forming the ith Slater determinant, $|\Phi_{\text{SD}}^{\alpha,i}\rangle$. The γ_{klmn} coefficients are obtained via antisymmetrization[c] of the spin-orbital combinations. One

[b] Note that for convenience we allow the index j on the spin orbitals χ_j mirror the electron index j on the electrons, but that the subset of spin orbitals $\{\chi_j\}$ is *different* for each Slater determinant. For a total set of $2K$ spin orbitals, one can generate $\binom{2K}{N}$ different determinants.

[c] To calculate the two-particle density matrix defined in Eq. (11) using GTOs one should antisymmetrize the combined wavefunction. The position of the electrons in the orbitals determines the sign of the product allowing the differ-

can see that the relation between one- and two-particle density matrices is different than in the Hartree-Fock case.[47,48]

Inserting Eq. (11) into Eq. (6), the expression for the dynamic structure factor becomes,

$$S(\mathbf{q}) = \sum_{i=1}^{N_{\text{conf}}} c_{\alpha,i}^2 \sum_{klmn}^{N_{\text{orb}}} \gamma_{klmn} \iint \phi_k^i(\mathbf{r}_1)\phi_l^i(\mathbf{r}_1)\phi_m^i(\mathbf{r}_2)\phi_n^i(\mathbf{r}_2)\, e^{i\mathbf{q}(\mathbf{r}_2-\mathbf{r}_1)}\, d\mathbf{r}_1 d\mathbf{r}_2, \tag{12}$$

where the orbital combinations are restricted to the non-vanishing two electron density matrix elements.[47] In the next section we shall consider the numerical evaluation of the matrix elements required to calculate $S(\mathbf{q})$ as in the equation above.

2.3 Evaluation of matrix elements

Evaluation of the combined Fourier transform on the right-hand side of Eq. (12) involves the expansion of the molecular orbitals $\{\phi_j^i(\mathbf{r})\}$ in a Gaussian basis $G_k(\mathbf{r})$,

$$\phi_j^i(\mathbf{r}) = \sum_{k=1}^{N_{\text{B}}} \mathcal{M}_k^j G_k(\mathbf{r}), \tag{13}$$

where $\mathcal{M}_k^j$ are the molecular orbital (MO) coefficients, N_{B} is the number of basis functions in the molecular orbital and $G_k(\mathbf{r})$ are the contracted basis functions. The $G_k(\mathbf{r})$ functions are expressed in terms of Gaussian type orbitals (GTOs), $g_s(\mathbf{r})$, which approximates a Slater basis for the MO,

$$G_k(\mathbf{r}) = \sum_{s=1}^{\mathfrak{n}_k} \mu_s^k\, g_s^k(\mathbf{r}), \tag{14}$$

with $\mathfrak{n}_k$ the number of contracted GTOs in $G_k(\mathbf{r})$ and μ_s^k the contraction coefficient for each GTO. The GTOs can be expressed in for instance spherical or Cartesian form,[49] and in the following we make use of Cartesian GTOs in the standard form,

$$g_A(\mathbf{r}) = \mathcal{N}_A (x-x_A)^{l_{Ax}} (y-y_A)^{l_{Ay}} (z-z_A)^{l_{Az}}\, e^{-\gamma_A(\mathbf{r}-\mathbf{r}_A)^2}, \tag{15}$$

representing a GTO with normalization constant $\mathcal{N}_A$, total angular momentum $l_A = l_{Ax} + l_{Ay} + l_{Az}$, exponent γ_A, and centered at $r_A = (x_A, y_A, z_A)$.

In order to evaluate Eq. (12), we substitute the $\phi_j^i(\mathbf{r})$ orbitals by their GTO expansion,

$$S(\mathbf{q}) = \sum_{i=1}^{N_{\text{conf}}} c_{\alpha,i}^2 \sum_{klmn}^{N_{\text{orb}}} \gamma_{klmn} \sum_{opqr}^{N_{\text{B}}} \sum_{abcd}^{\mathfrak{n}_{opqr}} \mathcal{M}_o^k \mathcal{M}_p^l \mathcal{M}_q^m \mathcal{M}_r^n \mu_a^o \mu_b^p \mu_c^q \mu_d^r \iint g_a^o(\mathbf{r}_1) g_b^p(\mathbf{r}_1) g_c^q(\mathbf{r}_2) g_d^r(\mathbf{r}_2)\, e^{i\mathbf{q}(\mathbf{r}_2-\mathbf{r}_1)}\, d\mathbf{r}_1 d\mathbf{r}_2, \tag{16}$$

where we have condensed the sums for simplicity, with the upper limit $\mathfrak{n}_{opqr} = \{\mathfrak{n}_o, \mathfrak{n}_p, \mathfrak{n}_q, \mathfrak{n}_r\}$. All the MO and contraction coefficients are independent of $\mathbf{r}_1$ and $\mathbf{r}_2$ and can thus be removed from the double-integral. The product of two GTOs can be simplified using the Gaussian product theorem,

$$g_a^o(\mathbf{r}) g_b^p(\mathbf{r}) = C_{op}\, e^{-\gamma_{op}(\mathbf{r}_1-\mathbf{r}_{op})^2} \tag{17}$$

with,

$$C_{op} = \exp\left(-\frac{\gamma_o\gamma_p}{\gamma_o+\gamma_p}|\mathbf{r}_o-\mathbf{r}_p|^2\right), \tag{18}$$

$$\gamma_{op} = \gamma_o + \gamma_p, \tag{19}$$

$$\mathbf{r}_{op} = \frac{\gamma_o\mathbf{r}_o + \gamma_p\mathbf{r}_p}{\gamma_o+\gamma_p} \tag{20}$$

where o and p are the sub-indices corresponding to the first and second GTO respectively and we have omitted the angular momentum components and the normalization constants. Substituting Eq. (17) into Eq. (16) and considering the Cartesian angular momentum components, $\zeta_A(\mathbf{r}) = (x-x_A)^{l_{Ax}}(y-y_A)^{l_{Ay}}(z-z_A)^{l_{Az}}$, the dynamic structure factor is given by,

$$S(\mathbf{q}) = \sum_{i=1}^{N_{\text{conf}}} c_{\alpha,i}^2 \sum_{klmn}^{N_{\text{orb}}} \gamma_{klmn} \sum_{opqr=1}^{N_{\text{B}}} \sum_{s=1}^{\mathfrak{n}_{opqr}} \mathcal{M}_o^k \mathcal{M}_p^l \mathcal{M}_q^m \mathcal{M}_r^n \epsilon_a^o \epsilon_b^p \epsilon_c^q \epsilon_d^r\, C_{op} C_{qr} \iint \zeta_o(\mathbf{r}_1)\zeta_p(\mathbf{r}_1)\zeta_q(\mathbf{r}_2)\zeta_r(\mathbf{r}_2)\, e^{-\gamma_{op}(\mathbf{r}_1-\mathbf{r}_{op})^2} e^{-\gamma_{qr}(\mathbf{r}_2-\mathbf{r}_{qr})^2} e^{i\mathbf{q}(\mathbf{r}_2-\mathbf{r}_1)} d\mathbf{r}_1 d\mathbf{r}_2, \tag{21}$$

ent antisymmetric products to be grouped, reducing the time required for the calculation of Eq. (12).

where we have combined the GTO contraction coefficients and normalization constants as $\epsilon_a^o = \mu_a^o \mathcal{N}_a$. The integrals on the right-hand side correspond to Fourier transforms of the Gaussian products in $\mathbf{r}_1$ and $\mathbf{r}_2$. Since the GTOs can be factorized in terms of the x, y and z Cartesian components, we can express the $\mathbf{r}_1$ and $\mathbf{r}_2$ components in the double-integral in Eq. (21) in the following product form,

$$\zeta_o(\mathbf{r})\zeta_p(\mathbf{r})\, e^{-\gamma_{op}(\mathbf{r}-\mathbf{r}_{op})^2} = \prod_{\lambda=x,y,z} (\lambda-\lambda_o)^{l_{o\lambda}}(\lambda-\lambda_p)^{l_{p\lambda}}\, e^{-\gamma_{op}(\lambda-\lambda_{op})^2}. \tag{22}$$

This factorization reduces the double-integral in Eq. (21) to a product of one-dimensional Fourier transforms as follows,

$$\begin{aligned}\iint \zeta_o(\mathbf{r}_1)\ldots e^{i\mathbf{q}(\mathbf{r}_2-\mathbf{r}_1)}\, d\mathbf{r}_1 d\mathbf{r}_2 = \\ \prod_{\lambda=x,y,z} \mathcal{F}_\lambda\left[(\lambda-\lambda_o)^{l_{o\lambda}}\,(\lambda-\lambda_p)^{l_{p\lambda}}\, e^{-\gamma_{op}(\lambda-\lambda_{op})^2}\right](\mathbf{q}) \\ \times \mathcal{F}_\lambda\left[(\lambda-\lambda_q)^{l_{q\lambda}}(\lambda-\lambda_r)^{l_{r\lambda}}\, e^{+\gamma_{qr}(\lambda-\lambda_{qr})^2}\right](\mathbf{q}).\end{aligned} \tag{23}$$

These Fourier transformations can be determined analytically, as has been shown and tabulated in previous publications.[30,33]

2.4 The Independent Atom Model

In the result section extensive comparisons are made to the Independent Atom Model (IAM) originally proposed by Debye.[50] This model is widely used across crystallography, not the least due to its considerable computational convenience. The IAM approximates the electron density as a sum of isotropic isolated-atom electron densities centered at the positions of the nuclei, which makes it possible to use tabulated[51] atomic form factors, $f_i^0(q)$, and inelastic corrections, $S_{\mathrm{inel},i}^{\mathrm{IAM}}(q)$, to express the total scattering as,

$$S_{\mathrm{IAM}}(\mathbf{q}) = \left|\sum_{i=1}^{N_{\mathrm{at}}} f_i^0(q)\, e^{\imath\mathbf{q}\mathbf{R}_i}\right|^2 + \sum_{i=1}^{N_{\mathrm{at}}} S_{\mathrm{inel},i}^{\mathrm{IAM}}(q), \tag{24}$$

where the sums run over all the N_{at} atoms in the molecule and $\mathbf{R}_i$ are the position vectors for the atoms. In the more familiar rotationally averaged form, Eq. (24) becomes,

$$S_{\mathrm{IAM}}(q) = \sum_{i,j}^{N_{\mathrm{at}}} f_i^0(q) f_j^0(q)\, \frac{\sin qR_{ij}}{qR_{ij}} + \sum_{i=1}^{N_{\mathrm{at}}} S_{\mathrm{inel},i}^{\mathrm{IAM}}(q), \tag{25}$$

where $R_{ij} = |\mathbf{R}_j - \mathbf{R}_i|$ is the distance between atoms i and j. In both expressions above, the first term corresponds to the elastic component and the second to the inelastic (which is identical in both expressions and which is considered to be independent of molecular geometry). The shortcomings in the IAM approximation for elastic scattering are well documented, and mainly relate to an inadequate description of the distortion of the electron density in molecules due to chemical bonding (see e.g. Refs.[30–32]). Arguably, the shortcomings for the inelastic component are greater, however in the context of crystallography the dominance of the elastic component serves to offset this.

3 Computational details

The wavefunctions used to obtain scattering cross sections are calculated using multireference configuration interaction (MRCI) with the choice of active space and basis specified in each case, and using canonical orbitals. MRCI accounts for much of the static electron correlation, as well as dynamic correlation, and provides an attractive compromise between computational resources and accuracy, making it possible attain reliable cross sections at affordable computational cost.

The CI configurations are expanded in configuration state functions (CSFs) for simplicity, expressing the spin populations as branches in a statistical sense in terms of spin quantum numbers. Matrix elements corresponding to the total scattering are pre-computed, accounting for antisymmetrization in the application of the two-particle density matrix operator to the wavefunctions.[52] These coefficients, combined with the configuration interaction vectors, are used to solve Eqs. (21) and (23).

The one- and two-particle density matrices are constructed from *ab-initio* MRCI outputs consid-

ering both diagonal and off-diagonal terms. Furthermore, in small systems, such as atoms or diatomic molecules, symmetry is useful to reduce the number of calculations required. We have used the electronic structure package MOLPRO[53] and a modified version of our recently developed *ab-initio* x-ray diffraction (AIXRD) code[30,33] to calculate total and elastic cross sections. Also note that the rotational averaging $\langle \cdots \rangle_\Omega$ is done numerically, but that analytical solutions are also possible.[54] Fig. 1 illustrates the relationship between the convergence of the rotational-averaging and the number of points used in the numerical integration in the H_2 molecule. The results from Bentley *et al.*[55] are used as the reference value, and all the differences shown are normalized. It is noted that at least 50 points per Euler angle are required to obtain a reliable rotational-averaging of the scattering signal.

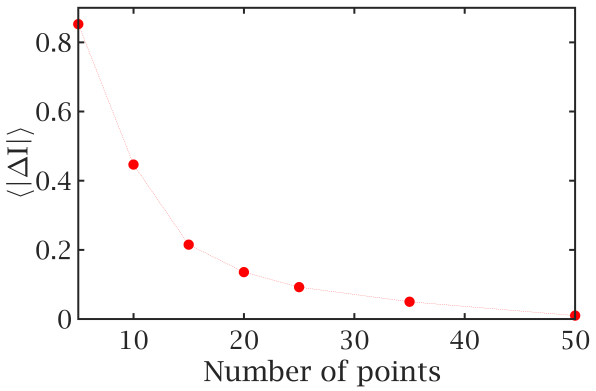

Figure 1: Rotational-average convergence of the total scattering as a function of the number of integration points in the H_2 molecule. The reference value is taken from Ref.[55]

When we compare results of different calculations in this article, we use the direct difference defined as,

$$\Delta I_{\{\text{total/elas/inel}\}}(q) = I_{\text{method}}(q) - I_{\text{ref}}(q), \qquad (26)$$

where the subscript refers to whether the cross-sections are for total, elastic or inelastic scattering, and the reference calculation, I_{ref}, is obtained using the highest level of theory available (largest active space and basis set). The corresponding percent difference is defined as,

$$\%\Delta I_{\{\text{total/elas/inel}\}}(q) = 100\frac{\Delta I_{\{\text{total/elas/inel}\}}(q)}{I_{\text{ref}}(q)}, \qquad (27)$$

with the integrated absolute percent difference,

$$\langle|\%\Delta I_{\{\text{total/elas/inel}\}}(q)|\rangle = \int_{q_{min}}^{q_{max}} |\%\Delta I_{\{\text{total/elas/inel}\}}(q)|\, dq. \qquad (28)$$

4 Results and Discussion

4.1 Total scattering from molecules

In this section we begin by validating our method against available experimental data and previous computations and establish reference calculations for the two molecules H_2 and CO_2. We then examine convergence with respect to the level of *ab-initio* theory used for the electronic structure calculations for various methods. We use multi-reference *ab-initio* methods to benchmark our calculations against previous results, but we note that the calculations could in principle also be carried out using a single-reference method such as CCSD(T).

4.1.1 H_2

The H_2 molecule is a well-established benchmark system both for experiments[56–59] and theory.[19–21,31,38,55,60–62] In Fig. 2, we show the calculated rotationally averaged total, elastic and inelastic scattering signals for the ground state H_2 molecule. Our *ab-initio* results are calculated at the MRCI(2,7)/aug-cc-pVTZ level of theory, with the bond length fixed at the geometry-optimized value of $R_{\text{HH}} = 0.7439$ Å. The calculations agree well with previous results shown in Fig. 2, both experimental elastic[56] and inelastic[57] scattering[d] and calculated total[19] and elastic.[31] The small difference between our present calculations and those performed by Bentley *et al.* is likely to be attributed to the lack of dynamical correlation in the

[d] Note that while the elastic component is taken from x-ray scattering, the inelastic component comes from high-energy electron scattering experiments.

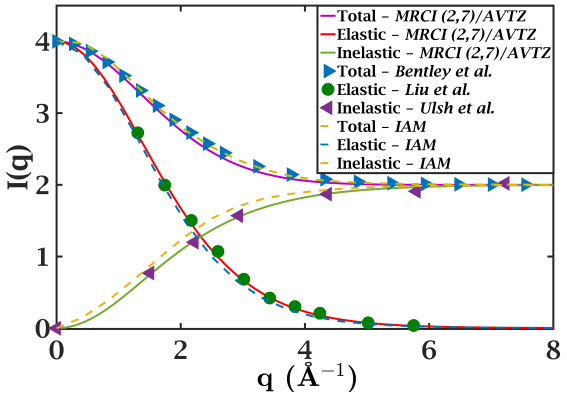

Figure 2: Total, elastic and inelastic scattering for the H_2 molecule, showing experimental results for elastic[56] and inelastic,[57] our own MRCI(2,7)/aug-cc-pVTZ-level calculations, previous *ab-initio* calculations of elastic[31] and total scattering,[19] and the independent atom model (IAM) results.

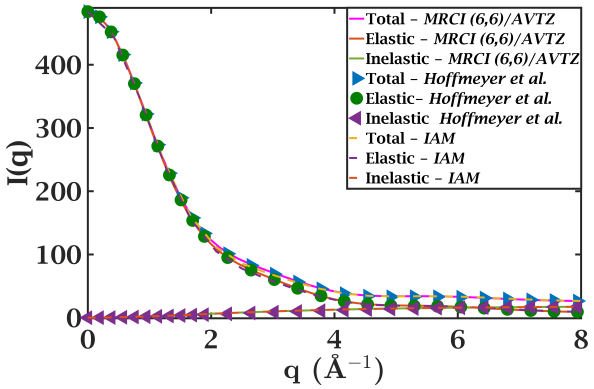

Figure 3: Total, elastic and inelastic scattering cross-sections for the CO_2 molecule in the ground state calculated at a MRCI(6,6)/AVTZ level of theory. Previous calculations by Hoffmeyer *et al.*[63] are also shown for comparison.

latter. The results shown in Fig. 2 also confirm the limiting behaviour of the total scattering S, the elastic scattering $S_{\text{elas}} = |F|^2$, and the inelastic scattering S_{inel} with respect to the momentum transfer q, as discussed in Section 2,

$$q = 0 \qquad \begin{cases} S &= 4 \quad (= N^2) \\ |F|^2 &= 4 \quad (= N^2) \\ S_{\text{inel}} &= 0 \end{cases}$$

$$q \to \infty \qquad \begin{cases} S &= 2 \quad (= N) \\ |F|^2 &= 0 \\ S_{\text{inel}} &= 2 \quad (= N) \end{cases} . \qquad (29)$$

where N is the number of electrons as before.

In agreement with previous studies,[31] the elastic scattering predicted by the independent atom model (IAM) deviates significantly from the correct result. This relates directly to the fact that *all* electrons in H_2 are valence electrons, since IAM performs better for molecules consisting of atoms with a larger number of core electrons.[30] It is notable, however, that the error in the inelastic component is even greater than the error in the elastic scattering. This in turn relates to the exceptionally poor description of electron correlation effects in IAM.

4.1.2 CO_2

Next we consider the significantly more challenging molecule CO_2. In Fig. 3 we show rotationally averaged total, elastic, and inelastic scattering cross sections (as in the case of H_2 above, the Thompson cross section is not included) for CO_2 in the ground state. The geometry is optimized at MRCI(6,6)/aug-cc-PVTZ^e level of theory, with the C-O distance $R_{\text{CO}} = 1.07$ Å and the molecule linear ($\Theta_{\text{OCO}} = 0°$). The calculated elastic, inelastic and total scattering are compared to previous MRCI results, obtained numerically by Hoffmeyer and coworkers.[63] The agreement is almost perfect. As before, the $q = 0$ and $q \to \infty$ limiting values follow the expectations summarized by Eq. (29). It is interesting to note that the IAM results show better agreement for CO_2 than H_2. The higher number of core electrons in CO_2 compensate to some extent for the poor description of the valence electrons in IAM. Having established in two different molecules that our method yields correct results, we now move on to investigate the convergence behaviour of the scattering calculation and, later, how the scattering cross sections depend on molecular geometry.

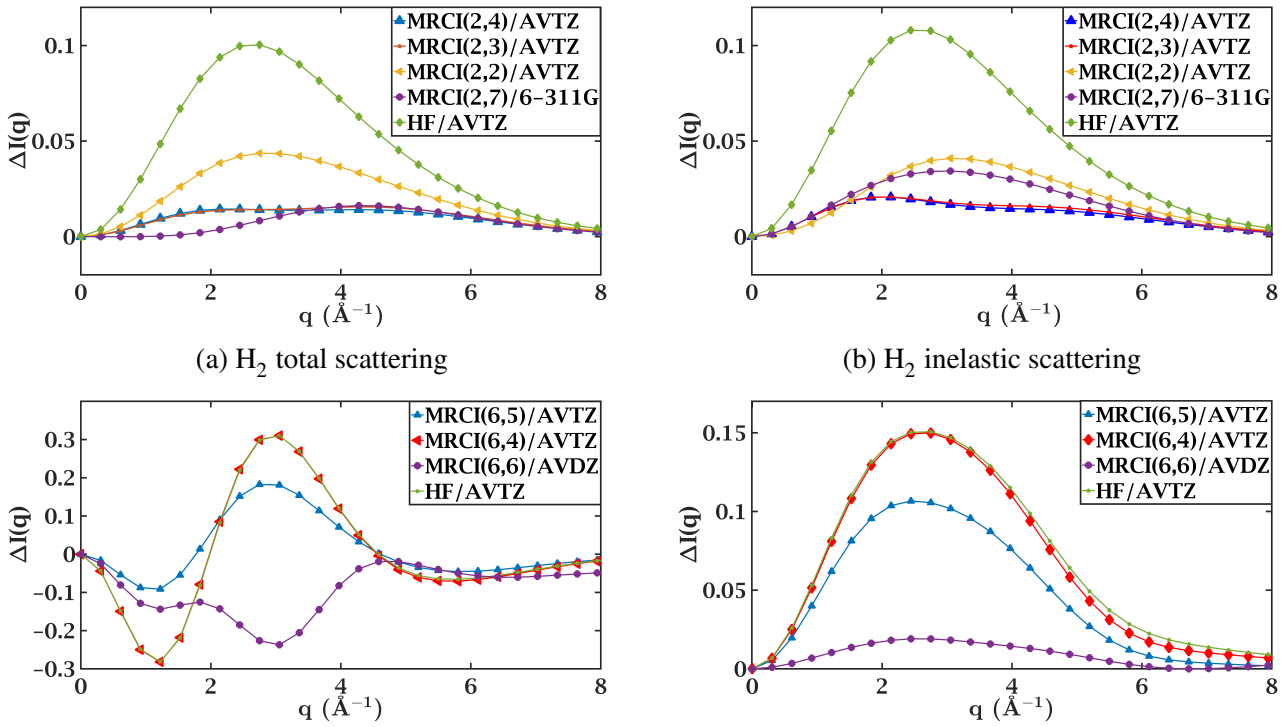

(a) H_2 total scattering

(b) H_2 inelastic scattering

(c) CO_2 total scattering

(d) CO_2 inelastic scattering

Figure 4: Calculated total and inelastic scattering patterns from H_2 (top row) and CO_2 (bottom row) at different levels of *ab-initio* theory, with total scattering in the left column and inelastic in the right. The signals are shown as the direct difference defined in Eq. (26), with MRCI(2,7)/AVTZ used as reference for H_2 and MRCI(6,6)/AVTZ for CO_2.

4.1.3 Convergence and method comparison

Using the reference calculations for the two molecules H_2 and CO_2 in Sections 4.1.1 and 4.1.2 above, we proceed to examine the convergence of the total and inelastic scattering with respect to the level of *ab-initio* theory, notably the size of the active space and the basis set when using MRCI, and contrast MRCI with Hartree-Fock (HF) level calculations and the independent atom model (IAM). The active spaces chosen are balanced to correctly account for static and dynamic electron correlation. In Fig. 4, we consider the direct difference (as defined by Eq. 26) for the total and inelastic scattering for a number of different model chemistries.

Starting with H_2, the results are shown in the top row of Fig. 4. Throughout, the MRCI(2,7)/AVTZ calculations are used as reference. We see in Fig. 4a that the total scattering is strongly influenced by the level of theory. As expected, the mean-field HF calculations show the greatest deviation from the reference total scattering curve. Introducing MRCI with the same basis as the HF calculations but with increasing active spaces $(2,2) \rightarrow (2,3) \rightarrow (2,4)$, improves electron correlation and we see that the signal improves as the active space increases, although the difference between the (2,3) and (2,4) active spaces is minimal. Strikingly, reducing the size of the basis to 6-311G in the reference MRCI(2,7) calculations yields results that are still quite good. At small q, which is dominated by the elastic scattering, the smaller basis yields a cross section almost as good as the larger AVTZ basis. At intermediate q the signal deteriorates, presumably due to a poorer description of correlation, but remains only slightly worse than the MRCI(2,3)/AVTZ and MRCI(2,4)/AVTZ results.

To shed further light on this, we examine the inelastic scattering, obtained by subtracting the elastic scattering from the total. This isolates the effect of electron correlation since the elastic component depends on the electron density and is thus a one-electron property. The direct differences relative to the reference calculations for the inelastic scattering are shown in Fig. 4b. The mean-field HF has the worst performance, as expected, and MRCI with increasing active space improves the results, although as before the difference between the (2,3) and (2,4) active spaces is slight. Reducing the size of the basis from AVTZ to 6-311G at the reference level of theory yields a more notable deterioration of the inelastic scattering than in the total scattering, with the result more or less on par with the smallest MRCI(2,2)/AVTZ calculation. This further emphasizes that the comparative overperformance of the 6-311G basis at small q for the total scattering shown in Fig. 4a is related to the electron density and the elastic scattering. On the other hand, the reduction in the number of Gaussian-type orbitals when going from AVTZ to 6-311G has a clear negative impact on the inelastic term.

Moving on to the CO_2 molecule, we see very similar trends as in H_2. The calculations from Section 4.1.2 are used as reference. The difference curves between the reference MRCI(6,6)/AVTZ calculations and the other model chemistries are shown in the bottom row of Fig. 4. The total scattering differences in Fig. 4c show the expected behaviour with HF performing on par with MRCI(6,4), which is not surprising given that the (6,4) active space is only a slight improvement on HF. Increasing the active space to (6,5) makes a significant improvement. Reducing the basis set in the reference MRCI(6,6) calculation from AVTZ to AVDZ reduced the accuracy about as much as reducing the active space from (6,6) to (6,5). Moving on the the inelastic scattering shown in Fig. 4d, we see HF perform almost identically to MRCI(6,4) at small and intermediate q, but degrades at larger q. Interestingly, the effect of reducing the basis set in the reference calculation from AVTZ to AVDZ is quite small, indicating that the reduction in basis size affects the elastic component more strongly in CO_2 than H_2.

Performing the same comparison as in Fig. 4, but now with respect to the independent atom model (IAM), we show in Fig. 5 the performance of IAM versus the reference calculations, with the MRCI(2,7)/6-311G (H_2) and MRCI(6,6)/AVDZ (CO_2) results from Fig. 4 included as a point of reference. As before, the top row shows the total and inelastic scattering differences calculated according to Eq. (26) for H_2 and likewise for CO_2 in the bottom row. The poor IAM results for the

[e] In the remainder of the article we use AVTZ for aug-cc-PVTZ, AVDZ for aug-cc-PVDZ, etc.

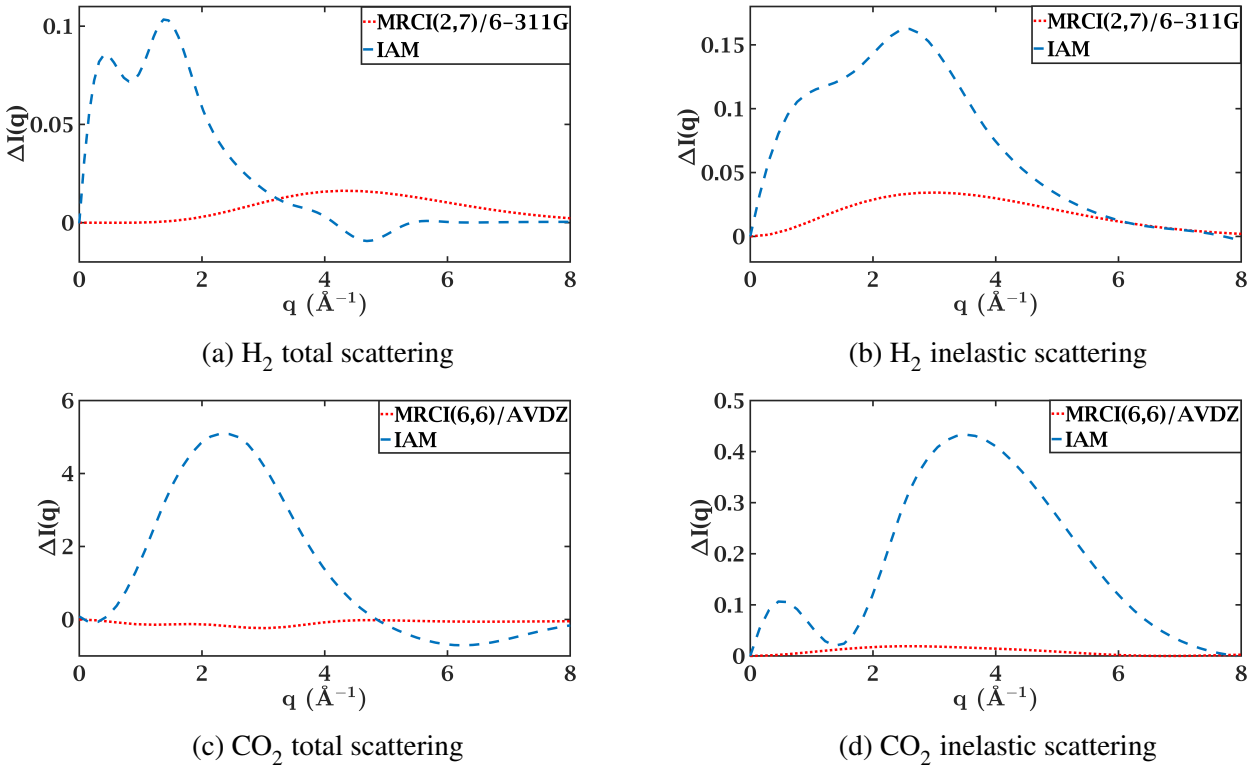

(a) H_2 total scattering

(b) H_2 inelastic scattering

(c) CO_2 total scattering

(d) CO_2 inelastic scattering

Figure 5: Comparison of the independent atom model (IAM) to the *ab-initio* cross sections for total (left column) and inelastic (right column) scattering, with H_2 in the top row and CO_2 in the bottom. The direct differences shown are calculated by Eq. (26) with MRCI(2,7)/AVTZ used as reference for H_2 and MRCI(6,6)/AVTZ for CO_2. The best-performing non-reference MRCI results from Fig. 4 are included for guidance.

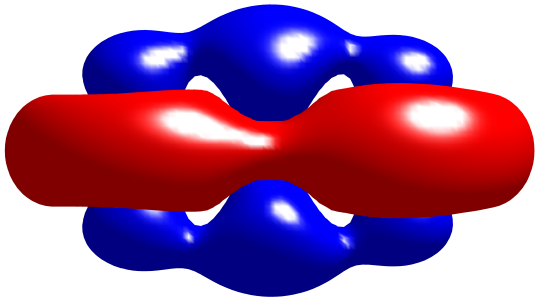

Figure 6: Isosurfaces (red negative, blue positive) for the electron density difference, $\triangle\rho = \rho_{\text{IAM}} - \rho_{\text{ab-initio}}$, between the IAM and the *ab-initio* electronic density calculated at the MRCI(6,6)/AVTZ level in the molecule CO_2.

total scattering is evident for both H_2 and CO_2 and relates to the poor description of the valence-bond electrons inherent in IAM (Figs. 5a and 5c). A measure of the deviation of the IAM electron density from the actual *ab-initio* electron density is given by Fig. 6, which shows isosurfaces for the electron density differences in CO_2. The density differences relate to the density associated with the bonding electrons, including the out-of-plane π-electrons. In Figs. 5b and 5d the inelastic scattering differences are shown instead. The error in the inelastic scattering is also significant, which is not surprising given that the Compton inelastic factors used in IAM are atomic, thus neglecting all molecular valence transitions and resulting in a poor description of inelastic scattering especially at small and intermediate values of q. It should also be noted that while the magnitude of the deviations is invariably greater for CO_2 than H_2, this simply reflects that the number of electrons in CO_2 is greater. However, as we shall see in the next paragraph, the percentage differences in H_2 can be very large.

In Table 1 we compare the accuracy of the calculated cross sections as a function of the level of theory, using the same results as already shown in Figs. 4 and 5. Integrated percent differences are calculated according to Eq. (28) for the total, elastic and inelastic scattering and are shown together with the relative energy convergence of each method relative the reference calculations. The energy convergence $|E - E_{ref}|$ ranks correctly the accuracy of the scattering calculations in both molecules, in accordance with previous observations.[31] The energy convergence relates to the accuracy of the wavefunction, which in turn directly influences the description of total and elastic scattering, and thus provides a general and reliable indicator of the expected quality of scattering calculations. We note that increasing the active space improves the results, while a decrease in the basis set increases the error. However, a correct description of electron correlation particularly influences the convergence of the inelastic scattering, which thus correlates strongly with the accuracy of the description of electron correlation in the two-particle density matrix, while the elastic scattering depends on the electron density and thus reflects the one-electron density matrix. It is notable that the convergence of the inelastic component is almost invariably poorer than the elastic component, with the MRCI(6,6)/AVDZ calculation in CO_2 the only exception. Since the total scattering contains contributions from both elastic and inelastic scattering, it is influenced by both the electron density and the correlation.

4.2 Geometry dependence of inelastic scattering

Here, we investigate the influence of molecular geometry on inelastic scattering. The inelastic component is commonly assumed to be constant, for instance in IAM, but we will show that it varies significantly with molecular geometry.

In Fig. 7 the dependence of the inelastic scattering on the molecular geometry in the molecules H_2 and CO_2 is demonstrated. The panels 7a and 7b show the change in inelastic scattering for H_2 as a function of the internuclear distance $0.5 < R_{\text{HH}} < 4$ Å, with the scattering calculated at the MRCI(2,7)/AVTZ level of theory. The inelastic scattering at the equilibrium bondlength $R_{\text{HH}}^{\text{eq}} = 0.74$ Å is used as reference. Panel 7a is an intensity plot of the percent difference as a function of R_{HH} and the momentum transfer q. In terms of the q dependence, the difference is strictly zero at $q = 0$ irrespective of R_{HH}, but is greatest at small and intermediate values of q, while it is negligible for $q > 6$ Å^{-1}. The change in inelastic scattering as a function of R_{HH} is also quite distinct.

Table 1: Accuracy and computational effort as a function of the level of theory for H_2 and CO_2. The integrated percent errors are calculated according to Eq. 28 for total, inelastic and elastic scattering over the interval $q \in [0,8]$ Å^{-1}. The energy convergence $|E - E_{\text{ref}}|$ relative to the reference calculations is used as a proxy for *ab-initio* convergence. The IAM calculations use tabulated atomic form factors.[51]

Method	ΔTotal(%)	ΔInel (%)	ΔElastic(%)	$\lvert E - E_{ref}\rvert 10^{-2} E_h$
		H_2		
IAM	18.0	57.0	34.8	–
HF/AVTZ	16.2	38.8	18.6	3.7
MRCI(2,4)/AVDZ	5.02	12.9	4.95	0.78
MRCI(2,2)/AVTZ	3.82	13.1	4.34	0.39
MRCI(2,3)/AVTZ	3.62	10.2	3.90	0.39
MRCI(2,4)/AVTZ	3.03	9.90	1.73	0.30
MRCI(2,7)/AVTZ	0.00	0.00	0.00	0.00
		CO_2		
IAM	8.43	15.4	8.66	–
HF/AVTZ	7.44	9.80	2.70	55.6
MRCI(6,6)/AVDZ	1.64	1.33	1.93	12.7
MRCI(6,4)/AVTZ	1.40	9.47	1.86	2.21
MRCI(6,5)/AVTZ	0.90	6.80	1.25	1.51
MRCI(6,6)/AVTZ	0.00	0.00	0.00	0.00

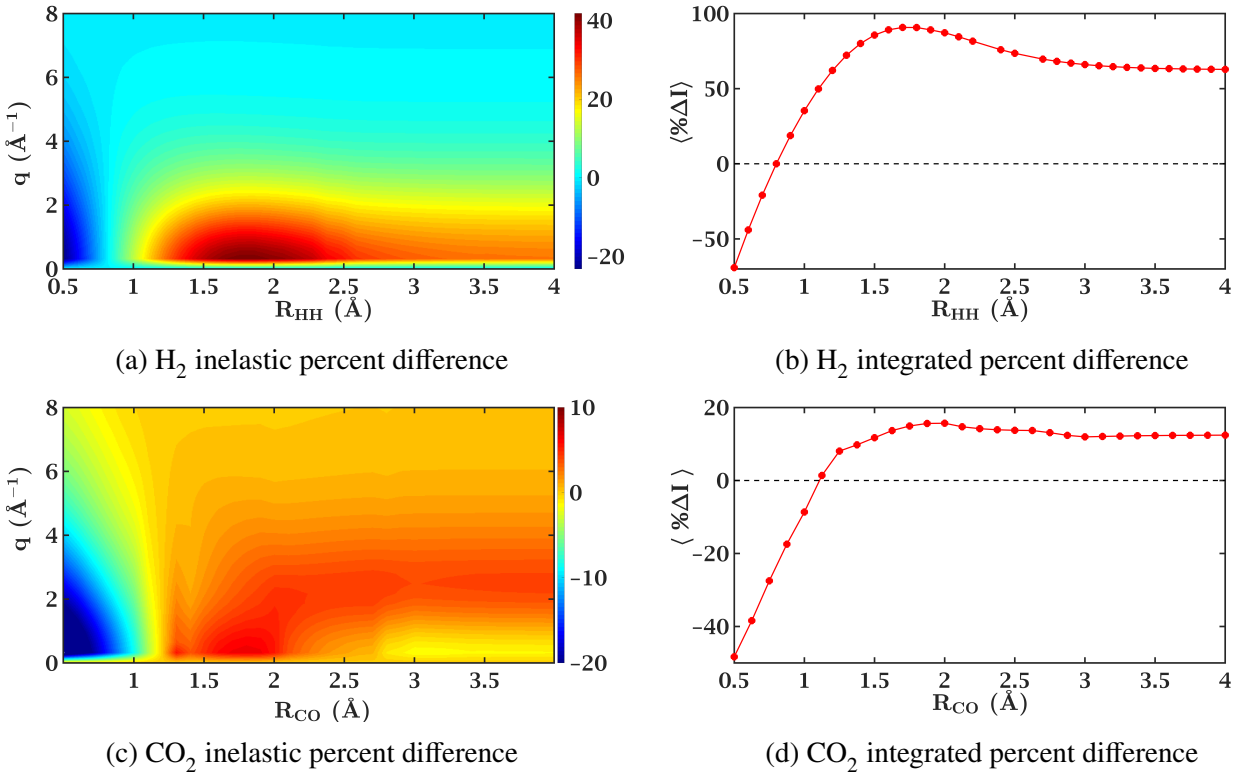

(a) H_2 inelastic percent difference

(b) H_2 integrated percent difference

(c) CO_2 inelastic percent difference

(d) CO_2 integrated percent difference

Figure 7: Geometry dependence of inelastic scattering, shown as percent differences relative the equilibrium geometry. The top row shows results for H_2, with the percent difference as a function of the momentum transfer q and the internuclear distance R_{HH} in the left panel and as the q-integrated $q \in [0,8]$ Å^{-1} percent difference in the right panel (according to Eq. 28 but without taking the absolute value). The bottom row shows the corresponding results for CO_2.

For $R_{HH} < R_{HH}^{eq}$, the inelastic scattering *decreases* while it *increases* for $R_{HH} > R_{HH}^{eq}$. This can be seen even more clearly in terms of the q-independent percent difference calculated according to Eq. (28) shown in panel 7b. The inelastic signal decreases by more than -56% towards $R_{HH} = 0.5$ Å and then increases for $R_{HH} > R_{HH}^{eq}$ to a maximum value of approximately +92% at $R_{HH} \sim 1.75$ Å to finally settle at approximately +63% for $R_{HH} > 3$ Å. The overall trend can be understood by considering the united atom $R_{HH} \to 0$ and the separated atom $R_{HH} \to \infty$ asymptotic limits, corresponding to a He atom and two H atoms respectively. The inelastic scattering from one He atom is distinctly less than that from two H atoms (see e.g. Table 7.4.3.2 in Ref.[51]), which can be related qualitatively to the significantly smaller energy splitting between the ground and excited states in H compared to He. The maximum at intermediate R_{HH} relates to the bonding region, where electron correlation leads to a comparatively strong multiconfigurational character that leads to greater inelastic scattering.

The behaviour observed in H_2 is echoed by the results for the CO_2 molecule shown in panels 7c and 7d. Panel 7c shows the change in inelastic scattering with respect to the C-O distance R_{CO} and the momentum transfer q, with the inelastic scattering at the equilibrium geometry (see Section 4.1.2) used as reference. One of the R_{CO} bondlengths is scanned from 0.5 to 3.0 Å, while the other is kept fixed at the equilibrium distance. The differences are again concentrated at small and intermediate values of q although they extend to larger q than for H_2. As before, the difference at $q = 0$ is strictly zero. At small values of R_{CO}, the inelastic components of the total scattering signal are smaller than at the equilibrium distance, down by -45% at $R_{CO} = 0.5$, and conversely the difference increases for $R_{CO} > R_{CO}^{eq}$ to a maximum of about +22% at approximately $R_{CO} = 1.9$ Å, however with a less distinct peak than what appears in H_2. In the asymptotic limit of large R_{CO}, the inelastic component becomes almost +20% larger than at the equilibrium geometry.

In Fig. 8 we compare the *ab-initio* geometry-dependent inelastic scattering in H_2 and CO_2 molecules to the tabulated IAM Compton factors

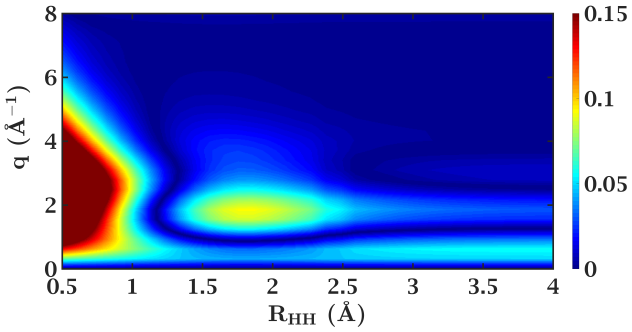

(a) H_2 inelastic IAM vs *ab-initio*

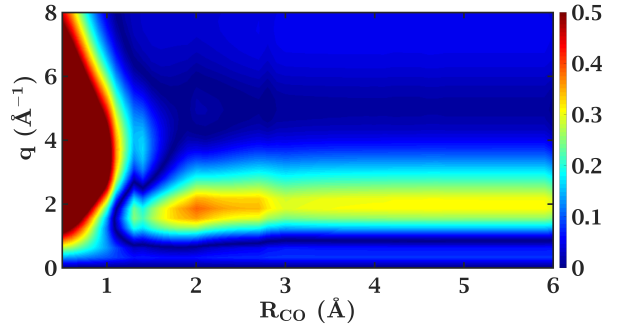

(b) CO_2 inelastic IAM vs *ab-initio*

Figure 8: Comparison of the geometry dependence of inelastic scattering for the *ab-initio* and the independent atom model (IAM), shown as an absolute difference, calculated according to Eq. (26), as a function of the bondlength R_{HH}/R_{CO} and the momentum transfer q. The top panel shows the results for H_2 and the bottom panel for CO_2, with the equilibrium geometry of each molecule used as reference.

in Ref.[51] Instead of showing the percent difference as in Fig. 7), we show here the absolute differences which convey the more subtle differences in this instance. Although the error at equilibrium geometry is reasonably small, the IAM values fail dramatically for small values of R_{HH} and R_{CO}. In the case of H_2, shown in panel 8a, the IAM works quite well in the separated atom limit, since the H-atom inelastic term is known very well. In CO_2, shown in panel 8b, a similar trend is observed, but in contrast a large difference between IAM and the *ab-initio* values persist for large R_{CO} since the *ab-initio* calculations are more accurate than tabulated terms, in particular for the CO fragment.

5 Conclusions

We present an *ab-initio* approach for the calculation of non-resonant total scattering, that is validated and benchmarked in the molecules H_2 and CO_2. The method is appropriate for the accurate prediction of total scattering cross sections for molecules in the gas-phase, probed by either x-rays or high-energy electrons, and could be matched with quantum molecular dynamics simulations for the interpretation of new ultrafast x-ray scattering and electron diffraction experiments.

The quality of the calculated cross sections relates to the accuracy of the wavefunction, with both the basis set and the level of theory exerting an influence. We demonstrate that a mean-field theory such as Hartree-Fock already improves on the independent atom model (IAM), especially in terms of the elastic component, but that multiconfigurational wavefunctions calculated with methods which better account for electron correlation are necessary to converge the total scattering. Although the differences between calculations using different levels of correlated *ab-initio* theory may appear subtle, these may nevertheless be important. In ultrafast scattering experiments, percent difference signals are used to cancel fluctuations in signal intensity[10] and the temporal changes in the percent difference are often on the order of a few percent, meaning that even small errors could potentially have an impact.

We further demonstrate that the inelastic component of the total scattering varies significantly once the nuclear positions are perturbed away from the equilibrium region. The dependence of the inelastic component on the molecular geometry is neglected in for instance the IAM approach, but could affect the interpretation of ultrafast scattering experiments tracking photochemical and photophysical processes, which often explore large regions of the potential energy landscape.

Looking ahead, it would be desirable to implement analytical rotational averaging, which should provide further significant computational savings. Since multiconfigurational approaches to electronic structure are appropriate for the calculation of electronically excited states in atoms and molecules, a natural next step for the work initiated in this article is to explore the total scattering cross sections for excited states. Another interesting direction is temperature effects due to vibrational corrections in high-resolution static gas-phase scattering experiments, which strictly speaking should be integrated coherently over vibrational and rotational states of the molecules.[21,32]

Acknowledgement A.K. acknowledges support from a Royal Society of Edinburgh Sabbatical Fellowship (58507) and, together with A.M.C., a research grant from the Carnegie Trust for the Universities of Scotland (CRG050414). P.M.W. acknowledges support by the U.S. Department of Energy, Office of Science, Basic Energy Sciences, under Award No. DE-SC0017995. H.Y. acknowledges funding from the Brown University Global Mobility Research Fellowship to support research visits at University of Canterbury and University of Edinburgh. P.M.W. acknowledges funding from the U.S. Department of Energy, Office of Science, Basic Energy Sciences, under Award No. DE-SC0017995. The computational work reported used the ARCHER UK National Supercomputing Service (http://www.archer.ac.uk), and support from the Edinburgh Parallel Computing Center (EPCC) is acknowledged.

References

(1) Galayda, J. N.; Arthur, J.; Ratner, D. F.; White, W. E. X-ray free-electron lasers–

present and future capabilities. *J. Opt. Soc. Am. B* **2010**, *27*, B106.

(2) Barty, A.; Küpper, J.; Chapman, H. N. Molecular Imaging Using X-Ray Free-Electron Lasers. *Ann. Rev. Phys. Chem.* **2013**, *64*, 415.

(3) Bostedt, C.; Bozek, J. D.; Bucksbaum, P. H.; Coffee, R. N.; Hastings, J. B.; Huang, Z.; Lee, R. W.; Schorb, S.; Corlett, J. N.; Denes, P.; Emma, P.; Falcone, R. W.; Schoenlein, R. W.; Doumy, G.; Kanter, E. P.; Kraessig, B.; Southworth, S.; Young, L.; Fang, L.; Hoener, M.; Berrah, N.; Roedig, C.; DiMauro, L. F. Ultra-fast and ultra-intense x-ray sciences: first results from the Linac Coherent Light Source free-electron laser. *J. Phys. B* **2013**, *46*, 164003.

(4) Feldhaus, J.; Krikunova, M.; Meyer, M.; Möller, T.; Moshammer, R.; Rudenko, A.; Tschentscher, T.; Ullrich, J. AMO science at the FLASH and European XFEL free-electron laser facilities. *J. Phys. B* **2013**, *46*, 164002.

(5) Yabashi, M.; Tanaka, H.; Tanaka, T.; Tomizawa, H.; Togashi, T.; Nagasono, M.; Ishikawa, T.; Harries, J. R.; Hikosaka, Y.; Hishikawa, A.; Nagaya, K.; Saito, N.; Shigemasa, E.; Yamanouchi, K.; Ueda, K. Compact XFEL and AMO sciences: SACLA and SCSS. *J. Phys. B* **2013**, *46*, 164001.

(6) Lyamayev, V.; Ovcharenko, Y.; Katzy, R.; Devetta, M.; Bruder, L.; LaForge, A.; Mudrich, M.; Person, U.; Stienkemeier, F.; Krikunova, M.; Möller, T.; Piseri, P.; Avaldi, L.; Coreno, M.; O'Keeffe, P.; Bolognesi, P.; Alagia, M.; Kivimäki, A.; Fraia, M. D.; Brauer, N. B.; Drabbels, M.; Mazza, T.; Stranges, S.; Finetti, P.; Grazioli, C.; Plekan, O.; Richter, R.; Prince, K. C.; Callegari, C. A modular end-station for atomic, molecular, and cluster science at the low density matter beamline of FERMI@Elettra. *J. Phys. B* **2013**, *46*, 164007.

(7) Choi, J.; Huang, J. Y.; Kang, H. S.; Kim, M. G.; Yim, C. M.; Lee, T.-Y.; Oh, J. S.; Parc, Y. W.; Park, J. H.; Park, S. J.; Ko, I. S.; Kim, Y. J. Design of the PAL XFEL. *J. Korean Phys. Soc.* **2007**, *50*, 1372.

(8) Minitti, M. P.; Budarz, J. M.; Kirrander, A.; Robinson, J. S.; Ratner, D.; Lane, T. J.; Zhu, D.; Glownia, J. M.; Kozina, M.; Lemke, H. T.; Sikorski, M.; Feng, Y.; Nelson, S.; Saita, K.; Stankus, B.; Northey, T.; Hastings, J. B.; Weber, P. M. Imaging molecular motion: Femtosecond x-ray scattering of an electrocyclic chemical reaction. *Phys. Rev. Lett.* **2015**, *114*, 255501.

(9) Minitti, M. P.; Budarz, J. M.; Kirrander, A.; Robinson, J.; Lane, T. J.; Ratner, D.; Saita, K.; Northey, T.; Stankus, B.; Cofer-Shabica, V.; Hastings, J.; Weber, P. M. Toward structural femtosecond chemical dynamics: imaging chemistry in space and time. *Faraday Discuss.* **2014**, *171*, 81–91.

(10) Budarz, J. M.; Minitti, M. P.; Cofer-Shabica, D. V.; Stankus, B.; Kirrander, A.; Hastings, J. B.; Weber, P. M. Observation of Femtosecond Molecular Dynamics via Pump-probe Gas Phase X-Ray Scattering. *J. Phys. B* **2016**, *49*, 034001.

(11) Stankus, B.; Budarz, J. M.; Kirrander, A.; Rogers, D.; Robinson, J.; Lane, T. J.; Ratner, D.; Hastings, J.; Minitti, M. P.; Weber, P. M. Femtosecond photodissociation dynamics of 1,4-diiodobenzene by gas-phase X-ray scattering and photoelectron spectroscopy. *Faraday Discuss.* **2016**, *194*, 525–536.

(12) Glownia, J. M.; Natan, A.; Cryan, J. P.; Hartsock, R.; Kozina, M.; Minitti, M. P.; Nelson, S.; Robinson, J.; Sato, T.; van Driel, T.; Welch, G.; Weninger, C.; Zhu, D.; Bucksbaum, P. H. Self-Referenced Coherent Diffraction X-Ray Movie of Ångström- and Femtosecond-Scale Atomic Motion. *Phys. Rev. Lett.* **2016**, *117*, 153003.

(13) Kim, K. H.; Kim, J. G.; Nozawa, S.; Sato, T.; Oang, K. Y.; Kim, T. W.; Ki, H.; Jo, J.;

Park, S.; Song, C.; Sato, T.; Ogawa, K.; Togashi, T.; Tono, K.; Yabashi, M.; Ishikawa, T.; Kim, J.; Ryoo, R.; Kim, J.; Ihee, H.; Adachi, S.-I. Direct observation of bond formation in solution with femtosecond X-ray scattering. *Nature* **2015**, *518*, 385–389.

(14) Yong, H.; Zotev, N.; Stankus, B.; Ruddock, J. M.; Bellshaw, D.; Boutet, S.; Lane, T. J.; Liang, M.; Carbajo, S.; Robinson, J. S.; Du, W.; Goff, N.; Chang, Y.; Koglin, J. E.; Waters, M. D. J.; Sølling, T. I.; Minitti, M. P.; Kirrander, A.; Weber, P. M. Determining Orientations of Optical Transition Dipole Moments Using Ultrafast X-ray Scattering. *J. Phys. Chem. Lett.* **2018**, *9*, 6556–6562.

(15) Minns, R. S.; Kirrander, A. Ultrafast Imaging of Photochemical Dynamics. *Faraday Disc.* **2016**, *194*, 11–13.

(16) Neutze, R.; Wouts, R.; Techert, S.; Davidsson, J.; Kocsis, M.; Kirrander, A.; Schotte, F.; Wulff, M. Visualizing Photochemical Dynamics in Solution through Picosecond X-Ray Scattering. *Phys. Rev. Lett.* **2001**, *87*, 195508.

(17) Bartell, L.; Gavin, R. Effects of Electron Correlation in X-Ray and Eiectron Diffraction. *J. Am. Chem. Soc.* **1964**, *86*, 3493–3498.

(18) Bartell, L.; Gavin, R. Effects of Electron Correlation in X-Ray and Electron Diffraction. II. Influence of Nuclear Charge in Two-Electron Systems. *J. Chem. Phys.* **1965**, *43*, 856–861.

(19) Bentley, J. J.; Stewart, R. F. Total x-ray scattering by H_2. *J. Chem. Phys.* **1975**, *62*, 875–878.

(20) Epstein, J.; Stewart, R. F. X-Ray and Electron Scattering from Diatomic Molecules in the First Born Approximation. *J. Chem. Phys.* **1977**, *66*, 4057–4064.

(21) Kołos, W.; Monkhorst, H. J.; Szalewicz, K. Energy unresolved differential cross section for electron scattering by H_2. *J. Chem. Phys.* **1982**, *77*, 1323–1334.

(22) Thakkar, A. J.; Tripathi, A. N.; Smith, V. H. Molecular x-ray- and electron-scattering intensities. *Phys. Rev. A* **1984**, *29*, 1108–1113.

(23) Bethe, H. Zur Theorie des Durchgangs schneller Korpuskularstrahlen durch Materie. *Ann. Phys.* **1930**, *397*, 325–400.

(24) Pirenne, M. H. *The Diffraction of X-rays and Electrons by Free Molecules*; Cambridge University Press, 1946.

(25) Inokuti, M. Inelastic Collisions of Fast Charged Particles with Atoms and Molecules: The Bethe Theory Revisited. *Rev. Mod. Phys.* **1971**, *43*, 297–347.

(26) Bonham, R. A.; Fink, M. *High Energy Electron Scattering*, acs monograph 169 ed.; Van Nostrand Reinhold Company, 1974.

(27) Ischenko, A. A.; Weber, P. M.; Miller, R. J. D. Capturing Chemistry in Action with Electrons: Realization of Atomically Resolved Reaction Dynamics. *Chemical Reviews* **2017**, *117*, 11066–11124.

(28) Centurion, M. Ultrafast imaging of isolated molecules with electron diffraction. *J. Phys. B* **2016**, *49*, 062002.

(29) Wolf, T. J. A.; Sanchez, D. M.; Yang, J.; Parrish, R. M.; Nunes, J. P. F.; Centurion, M.; Coffee, R.; Cryan, J. P.; Gühr, M.; Hegazy, K.; Kirrander, A.; Li, R. K.; Ruddock, J.; Shen, X.; Veccione, T.; Weathersby, S. P.; Weber, P. M.; Wilkin, K.; Yong, H.; Zheng, Q.; Wang, X. J.; Minitti, M. P.; Martínez, T. J. Imaging the Photochemical Ring-Opening of 1,3-Cyclohexadiene by Ultrafast Electron Diffraction. *Nat. Chem. / arXiv[physics.chem-ph]1810.02900* **2019**,

(30) Northey, T.; Zotev, N.; Kirrander, A. *Ab Initio* Calculation of Molecular Diffraction. *J. Chem. Theory Comput.* **2014**, *10*, 4911–4920.

(31) Northey, T.; Carrascosa, A. M.; Schäfer, S.; Kirrander, A. Elastic X-ray scattering from state-selected molecules. *J. Chem. Phys.* **2016**, *145*, 154304.

(32) Carrascosa, A. M.; Northey, T.; Kirrander, A. Imaging rotations and vibrations in polyatomic molecules with X-ray scattering. *Phys. Chem. Chem. Phys.* **2017**, *19*, 7853–7863.

(33) Carrascosa, A. M.; Kirrander, A. *Ab initio* calculation of inelastic scattering. *Phys. Chem. Chem. Phys.* **2017**, *19*, 19545–19553.

(34) Lorenz, U.; Møller, K. B.; Henriksen, N. E. Theory of time-resolved inelastic x-ray diffraction. *Phys. Rev. A* **2010**, *81*, 023422.

(35) Dixit, G.; Santra, R. Role of electron-electron interference in ultrafast time-resolved imaging of electronic wavepackets. *J. Chem. Phys.* **2013**, *138*, 134311.

(36) Simmermacher, M.; Henriksen, N. E.; Møller, K. B. Time-resolved X-ray scattering by electronic wave packets: analytic solutions to the hydrogen atom. *Phys. Chem. Chem. Phys.* **2017**, *19*, 19740–19749.

(37) Kirrander, A.; Saita, K.; Shalashilin, D. V. Ultrafast X-ray Scattering from Molecules. *J. Chem. Theory Comput.* **2016**, *12*, 957–967.

(38) Simmermacher, M.; Henriksen, N. E.; Møller, K. B.; Moreno Carrascosa, A.; Kirrander, A. Electronic Coherence in Ultrafast X-Ray Scattering from Molecular Wave Packets. *Phys. Rev. Lett.* **2019**, *122*, 073003.

(39) Debnarova, A.; Techert, S. *Ab initio* treatment of time-resolved x-ray scattering: Application to the photoisomerization of stilbene. *J. Chem. Phys.* **2006**, *125*, 224101.

(40) Debnarova, A.; Techert, S.; Schmatz, S. *Ab initio* studies of ultrafast x-ray scattering of the photodissociation of iodine. *J. Chem. Phys.* **2010**, *133*, 124309.

(41) Debnarova, A.; Techert, S.; Schmatz, S. Computational studies of the x-ray scattering properties of laser aligned stilbene. *J. Chem. Phys.* **2011**, *134*, 054302.

(42) Schülke, W. *Electron Dynamics by Inelastic X-Ray Scattering*, 1st ed.; Oxford Science Publications, 2007.

(43) Waller, I.; Hartree, D. R. On the Intensity of Total Scattering of X-Rays. *Proc. R. Soc. Lond. Ser.-A* **1929**, *124*, 119–142.

(44) Parrish, R. M.; Martínez, T. J. Ab Initio Computation of Rotationally-Averaged Pump-Probe X-ray and Electron Diffraction Signals. *J. Chem. Theory Comp.* **2019**, *X*, (accepted), PMID: 30702882.

(45) Stefanou, M.; Saita, K.; Shalashilin, D. V.; Kirrander, A. Comparison of Ultrafast Electron and X-Ray Diffraction A Computational Study. *Chem. Phys. Lett.* **2017**, *683*, 300–305.

(46) Watanabe, N.; Hayashi, H.; Udagawa, Y.; Ten-no, S.; Iwata, S. Static structure factor and electron correlation effects studied by inelastic x-ray scattering spectroscopy. *J. Chem. Phys.* **1998**, *108*, 4545–4553.

(47) Helgaker, T.; Jørgensen, P.; Olsen, J. *Molecular Electronic-Structure Theory*, 1st ed.; John Wiley and Sons, 2000.

(48) Szabo, A.; Ostlund, N. S. *Modern Quantum Chemistry: Introduction to Advanced Electronic Structure Theory*, 2nd ed.; Dover Publishing Inc., 1996.

(49) Schlegel, H. B.; Frisch, M. J. Transformation Between Cartesian and Pure Spherical Harmonic Gaussians. *Int. J. Quant. Chem.* **1995**, *54*, 83–87.

(50) Debye, P. Zerstreuung von Röntgenstrahlen. *Ann. Phys.* **1915**, *46*, 809.

(51) *International Tables for Crystallography Volume C: Mathematical, physical and chemical tables*; Wiley, 2006.

(52) Yarkony, D. *Modern Electronic Structure Theory*, 1st ed.; World Scientific, 1995; Advanced series in physical chemistry.

(53) Werner, H.-J.; Knowles, P. J.; Knizia, G.; Manby, F. R.; Schütz, M. MOLPRO, version 2012.1, a package of ab initio programs.

(54) Wang, J.; Smith, V. H. Evaluation of cross sections for X-ray and high-energy electron scattering from molecular systems. *Int. J. Quant. Chem.* **1994**, *52*, 1145–1151.

(55) Bentley, J.; Stewart, R. F. Two-Center Calculations for X-Ray Scattering. *J. Comp. Phys.* **1973**, *11*, 127.

(56) Liu, Y.-W.; Mei, X.-X.; Kang, X.; Yang, K.; Xu, W.-Q.; Peng, Y.-G.; Hiraoka, N.; Tsuei, K.-D.; Zhang, P.-F.; Zhu, L.-F. Determination of the electronic structure of atoms and molecules in the ground state: Measurement of molecular hydrogen by high-resolution x-ray scattering. *Phys. Rev. A* **2014**, *89*, 014502.

(57) Ulsh, R. C.; Wellenstein, H. F.; Bonham, R. A. Bethe surface, elastic and inelastic differential cross sections, Compton profile, and binding effects for H_2 obtained by electron scattering with 25 keV incident electrons. *J. Chem. Phys.* **1974**, *60*, 103–111.

(58) Xu, L.-Q.; Kang, X.; Peng, Y.-G.; Xu, X.; Liu, Y.-W.; Wu, Y.; Yang, K.; Hiraoka, N.; Tsuei, K.-D.; Wang, J.-G.; Zhu, L.-F. Comparative study of inelastic squared form factors of the vibronic states of $B\,^1\Sigma_u^+$, $C\,^1\Pi_u$, and $EF\,^1\Sigma_g^+$ for molecular hydrogen: Inelastic x-ray and electron scattering. *Phys. Rev. A* **2018**, *97*, 032503.

(59) Ibrahim, H.; Lefebvre, C.; Bandrauk, A. D.; Staudte, A.; Légaré, F. H_2 : the benchmark molecule for ultrafast science and technologies. *J. Phys. B* **2018**, *51*, 042002.

(60) Stewart, R. F.; Davidson, E. R.; Simpson, W. T. Coherent X-Ray Scattering for the Hydrogen Atom in the Hydrogen Molecule. *J. Chem. Phys.* **1965**, *42*, 3175.

(61) A. Kirrander and Ch. Jungen and H. H. Fielding, Localization of electronic wave packets in H_2. *J. Phys. B* **2008**, *41*, 074022.

(62) A. Kirrander and Ch. Jungen, Molecular ion-pair states in ungerade H_2. *Phys. Rev. A* **2011**, *84*, 052512.

(63) Hoffmeyer, R. E.; Bündgen, P.; Thakkar, A. J. Cross sections for x-ray and high-energy electron scattering by small molecules. *J. Phys. B* **1998**, *31*, 3675–3692.

Graphical TOC Entry